TRANSITION TO TURBULENCE IN AN INCOMPRESSIBLE FLOW PAST A MULTI-ELEMENT AIRFOIL: GÖRTLER VORTICES

Ming Teng
Barcelona Supercomputing Center
Plaça d'Eusebi Güell, 1-3, Les Corts, 08034 Barcelona
ming.teng@uottawa.ca

Catherine Mavriplis
Department of Mechanical Engineering
University of Ottawa
161 Louis-Pasteur Private, Ottawa, ON K1N 1A2, Canada
catherine.mavriplis@uottawa.ca

ABSTRACT

A direct numerical simulation database of incompressible flow past a high-lift airfoil (Teng and Mavriplis, *Int. J. Heat Fluid Flow* 115, 109825, 2025), obtained with a high-order spectral element method, is analyzed. The database comprises three cases at low chordwise Reynolds numbers, Re_c, with a fixed 4° angle of attack. Spectral proper orthogonal decomposition (SPOD) is used for modal analysis. For the $Re_c = 1.270 \times 10^4$ case, the most energetic structures occur at $St = fc/U_\infty = 0.8,\ 1.5$, and 2.3. For the $Re_c = 1.830 \times 10^4$ case, they occur at $St = 0.9$, 9.8, and 19.7. The SPOD modes reveal a reorganization of the dominant flow structures with Re_c. At $Re_c = 1.270 \times 10^4$, the low-frequency modes extend from the slat cove into the region above the main element, with peak amplitude near the interaction between the slat wake and the main-element boundary layer, while the higher-frequency modes become progressively more localized within the slat cove and near the slat trailing edge. In contrast, at $Re_c = 1.830 \times 10^4$, the dominant low-frequency mode is largely confined within the slat cove, suggesting a more localized oscillatory pattern. At higher frequencies, the modes exhibit convecting structures aligned with the shear layer separated from the slat cusp, consistent with Kelvin–Helmholtz instability. A direct link between the dominant energetic modes and centrifugal instability, however, is not evident from the present modal analysis.

INTRODUCTION

Wang *et al.* (2018) investigated the coherent flow structures of incompressible flow past the 30P30N high-lift airfoil at a chordwise Reynolds number $Re_c = U_\infty c/\nu = 0.832 \times 10^4$ and angles of attack $\alpha = 0°$–$16°$ in an experimental setting (U_∞ and c denote the freestream velocity and the stowed chord length of the airfoil, respectively; ν is kinematic viscosity). They observed regular longitudinal counter-rotating vortices over the leading edge of the main element for $2.0° \leq \alpha \leq 12.0°$, and, based on the inviscid Rayleigh criterion, conjectured that these were Görtler vortices generated by the shear layer emanating from the slat cove. A standard proper orthogonal decomposition (POD) analysis by Kokash *et al.* (2024) at $Re_c = 1.27 \times 10^4$ points instead to the slat cusp region, suggesting that the strong curvature of the flow around and downstream of the cusp is responsible for the observed Görtler vortices. Teng & Mavriplis (2025) implemented direct numerical simulations (DNS) and considered three low Re_c: 0.8320×10^4, 1.270×10^4 and 1.830×10^4. Both the inviscid Rayleigh criterion and the Görtler number were applied, each identifying regions of strong centrifugal effects but with limited overlap. While the Rayleigh criterion points to instability in the region extending from beneath to downstream of the slat trailing edge, the Görtler number instead indicates that instability is more likely to develop immediately aft of the slat cusp or within the recirculation region extending toward the slat trailing edge. Motivated by the uncertainties mentioned above, the present work aims to uncover key spectral and modal features of the flow field near the slat cove, linking them to the dominant instability mechanisms through spectral proper orthogonal decomposition (SPOD).

An advantage of SPOD over standard POD is that its modes vary in both space and time, being orthogonal with respect to a space–time inner product rather than a purely spatial one. This makes SPOD particularly effective in capturing spatiotemporal coherence in the data. It may be regarded as a special case of a broader space–time decomposition, assuming statistically stationary data (Schmidt *et al.*, 2018). For statistically stationary processes, SPOD integrates the strengths of dynamic mode decomposition (DMD)—its capacity to represent temporal correlations in coherent structures—with the optimality of POD in extracting energy-ranked modes (Schmidt & Colonius, 2020).

In comparison with applications in turbulent flow scenarios, SPOD applications in transiton to turbulence remain less common. Sasaki *et al.* (2020) developed and tested optimized actuators for closed-loop control of streaks induced by freestream turbulence in transitional boundary layers. All designs delayed transition and reduced drag, with up to 21% reduction; the best performance comes from the actuator reproducing the leading SPOD mode, as it most effectively cancels boundary-layer structures.

Lin & Schmidt (2024) implemented a modal analysis of a Klebanoff regime of transition scenario over a flat plate using

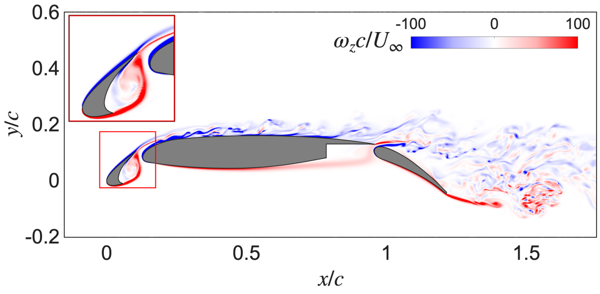

Figure 1. Slat-cove region for SPOD analysis highlighted with a red box and instantaneous spanwise vorticity, $\omega_z c/U_\infty$, for $Re_c = 1.830 \times 10^4$.

a DNS database. Multiple modal decomposition methodologies were employed to examine the dominant coherent structures associated with corresponding instability mechanisms throughout the transition process. SPOD-based analysis revealed flow features characteristic of transition via the Klebanoff regime prior to the onset of turbulence.

Aguirre *et al.* (2025) investigated boundary-layer transition over an open cavity in subsonic flow using DNS, linear stability theory (LST), and SPOD, highlighting the role of cavity-induced instabilities in promoting onset of transition. Both two-dimensional (2D) Rossiter and 3D centrifugal modes were identified, with LST predicting their frequencies and modal characteristics. SPOD analysis confirmed the presence of these modes and revealed spatial structures consistent with LST predictions at matching frequencies. DNS results showed the development of Λ-vortices downstream of the cavity, indicating flow destabilisation driven by cavity-shed disturbances. While Rossiter modes persisted into transitional and turbulent regions and contributed significantly to energy amplification, their 2D nature suggested that interaction with centrifugal instabilities was required for fully 3D flow development.

The present work extends a previous numerical simulation study of incompressible flow past a 30P30N high-lift configuration (Teng & Mavriplis, 2025) focusing on modal analysis using SPOD. In particular, this work seeks to assess whether the observed structures near the leading edge of the main element correspond to Görtler vortices and to identify their origin. Two low Re_c are considered, namely, $Re_c = 1.270 \times 10^4$ and 1.830×10^4. The analysis focuses on the slat-cove region where the centrifugal instability was previously identified using both the inviscid Rayleigh discriminant and Görtler number.

DNS DATABASE

The database used in this study is obtained from a series of 3D DNS of incompressible flow past a high-lift airfoil in a 30P30N configuration (Teng & Mavriplis, 2025). The database includes three low Re_c cases: 0.832×10^4, 1.270×10^4, and 1.830×10^4, all at a fixed angle of attack of 4.0°. The computational domain has a size of $x \times y \times z = 9c \times 5c \times 0.2c$ with z denoting the spanwise direction. More than 3.32×10^5 elements are employed, within each of which the solution is represented by tensor products of $7^{th}-$order polynomials in each direction, yielding a number of degrees of freedom of approximately 1.14×10^8. Figure 1 gives an overview of the flow field and the region for SPOD analysis. The origin of the coordinate system is placed at the leading edge of the slat when flow approaches at $\alpha = 0^\circ$.

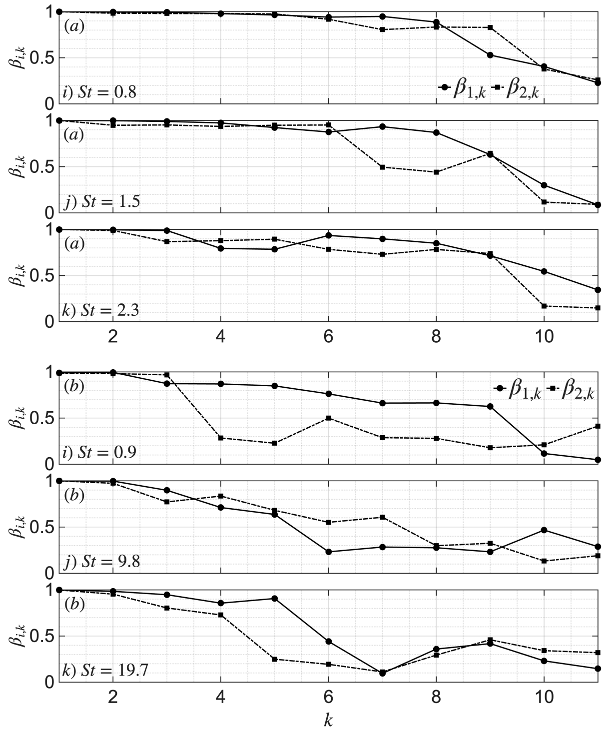

Figure 3. Convergence of the SPOD modes at the dominant frequencies for each Re_c case: (a) $Re_c = 1.270 \times 10^4$ $i)$ $St = 0.8$ $j)$ $St = 1.5$ $k)$ $St = 2.3$ and (b) $Re_c = 1.830 \times 10^4$ $i)$ $St = 0.9$ $j)$ $St = 9.8$ $k)$ $St = 19.7$. $\beta_{i,k}$ denotes the normalised projection of the k^{th} mode of the full dataset onto the corresponding mode of the i^{th} subset at a given frequency.

The results of the database were obtained by solving the Navier–Stokes equations using NekRS (Fischer *et al.*, 2022), a high-order spectral element method (Patera, 1984) optimized for GPU acceleration and equipped with highly scalable algorithms. These simulations followed the experiments of Wang *et al.* (2018) and demonstrated satisfactory agreement—both qualitatively and quantitatively—with the measurements documented in Wang *et al.* (2018); Wang & Wang (2021).

MODAL DECOMPOSITION

To identify the coherent structures associated with the dominant frequencies, SPOD is applied to the fluctuating velocity components, $u_i' = u_i - \langle u_i \rangle$ (u_i is the instantaneous velocity component and $\langle \cdot \rangle$ denotes temporal and spanwise-averaging operator). Therefore, the norm used here corresponds to the turbulent kinetic energy. The power spectral density (PSD) in the subdomain, see Fig. 2 for the chosen slat-cove region subdomain, exhibits dominant frequencies corresponding to a Strouhal number $St = fc/U_\infty < 32$ (where f is the frequency); a detailed discussion will be given in the RESULTS section. A sampling rate of $f_s = 64Hz$, corresponding to a maximum resolvable frequency of $f_{max} = 32Hz$ ($St_{max} = 32$), is therefore used to ensure the capture of relevant structures. Data spanning 80 time units T ($T = tU_\infty/c$ with t denoting the time for a particle to travel a distance c) are collected, resulting in a total of 5120 snapshots. A bin size of $\Delta f = 0.1Hz$ is used along with a best-practice 50% overlap between successive data blocks, yielding a total of 15 blocks. Each block contains 640 snapshots. A comparison was performed with results obtained using a 75% overlap (yielding 29 blocks). Discrepancies in both eigenvalues and SPOD modes

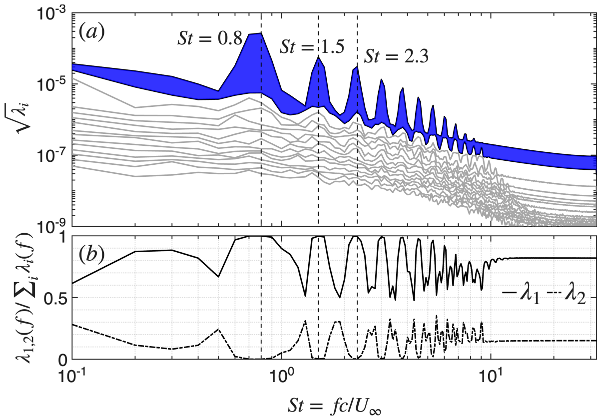

Figure 4. (a) SPOD energy spectra and (b) energy content associated with the first two modes for incompressible flow in the slat-cove region of a 30P30N high-lift airfoil (see Fig. 1) at $Re_c = 1.270 \times 10^4$. The vertical dashed lines (— — —) show three dominant frequencies: $St = fc/U_\infty = 0.8,\ 1.5$ and 2.3. The separation between the first and the second eigenvalues, $\sqrt{\lambda_1}$ and $\sqrt{\lambda_2}$, is highlighted in blue.

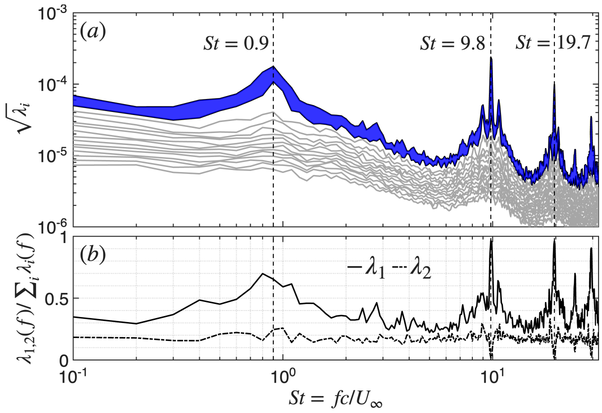

Figure 5. (a) SPOD energy spectra (b) energy content associated with the first two modes for incompressible flow in the slat-cove region of a 30P30N high-lift airfoil (see Fig. 1) at $Re_c = 1.830 \times 10^4$. The vertical dashed lines (— — —) show three dominant frequencies: $St = fc/U_\infty = 0.9,\ 9.8$ and 19.7. The separation between the first and the second eigenvalues, $\sqrt{\lambda_1}$ and $\sqrt{\lambda_2}$, is highlighted in blue.

are negligible, though a minor increase in uncertainty level is observed in both cases. A standard Hanning window is applied to minimize the spectral leakage.

A convergence study is first performed to validate the computation. Following the approach of Abreu *et al.* (2021), the dataset is divided into two subsets with identical snapshots overlapping by 50%, each representing 75% of the original dataset. SPOD is applied to both subsets and the full dataset, and a correlation coefficient can be defined as:

$$\beta_{i,k} = \frac{\langle \psi_k, \psi_{i,k} \rangle}{||\psi_k|| \cdot ||\psi_{i,k}||}, \quad (1)$$

where $\langle \cdot, \cdot \rangle$ denotes the standard L_2 inner product, and $|| \cdot ||$ represents the associated L_2 norm. The coefficient, $\beta_{i,k}$, therefore represents the normalised projection of the k^{th} mode of the full dataset, ψ_k, onto the corresponding mode of the i^{th} subset, $\psi_{i,k}$, at a given frequency. A unity correlation coefficient indicates an exact alignment between two modes whereas a zero signifies that the modes are orthogonal. The coefficients for the modes at the dominant frequencies are shown in Fig. 3. For both cases, the first two SPOD modes are consistent and found to be converged, with a coefficient $\beta_{i,k} \sim 0.95$.

RESULTS

Figure 2 presents the normalized PSD of streamwise velocity component, u, at selected locations near and within the slat cove for both Re_c cases. The regions where the flows are susceptible to strong centrifugal effects are also shown (see Fig. 2 (i) and (ii)), identified using the inviscid Rayleigh criterion and the Görtler number, $Gö_{\delta^*}$ (Teng & Mavriplis, 2025). The effect of Re_c is reflected in the energy spectrum and a shift of the dominant frequencies. For $Re_c = 1.270 \times 10^4$, distinct peaks are observed across the selected locations at $St < 10$ whereas in the higher-frequency region, the PSD exhibits a smooth spectral distribution. In contrast, the $Re_c = 1.830 \times 10^4$ case exhibits a broadband spectrum. The slopes evolve as flow circulates along the internal wall, separates at the cusp and emanates from the gap (see Fig. 2 $b-h$). Distinct frequency peaks become pronounced after separation at the slat cusp (see Fig. 2 $e-h$).

Figures 4 and 5 present the SPOD energy spectra and the energy content for two eigenvalues associated with the leading and second modes. A large separation is observed in both Re_c cases, highlighted in blue (see Figs 4(a) and 5(a)). It indicates the presence of the so-called low-rank behaviour in the flow, suggesting the presence of dominant mechanisms and highly energetic leading modes compared to the subdominant ones (Schmidt & Colonius, 2020). For the $Re_c = 1.270 \times 10^4$ case, see Figs 4(b), the energy content of subdominant modes at the peak frequencies is nearly negligible. A similar trend is also observed for $Re_c = 1.830 \times 10^4$, except at $St = 0.9$ (see Figs 5(b)), where the second mode captures $\sim 25\%$ energy as compared to $\sim 65\%$ for the first mode.

The dominant frequencies for the $Re_c = 1.270 \times 10^4$ case are identified at $St = 0.8,\ 1.5$ and 2.3, as shown in Fig. 4(a). The corresponding SPOD modes are shown in Fig. 6. The leading and subdominant modes at $St = 0.8$ are qualitatively consistent, as both capture coherent structures within the slat cove and downstream the gap, see Fig. 6(a,d), although they differ in detailed phase organization and distribution of modal amplitude. A low frequency at $St = 0.8$ is typically associated with a Kelvin-Helmholtz instability of a shear layer separating at the slat cusp. However, the corresponding SPOD modes indicate that this unsteadiness is not confined to the slat cove, but instead forms part of a coupled slat-wake and boundary-layer interaction, with the strongest amplification occurring downstream of the slat trailing edge near the main-element leading edge. The leading modes at $St = 1.5$ and 2.3 differ primarily in amplitude as shown in Fig. 6(b,c). A similarity in pattern is also observed in the corresponding subdominant modes (Fig. 6(e,f)). At $St = 1.5$, the SPOD modes exhibit more localized structures concentrated within the slat cove and near the slat trailing edge. The alternating pattern within the cove is likely associated with a vortex formation.

For the $Re_c = 1.830 \times 10^4$ case, the dominant frequencies are identified at $St = 0.9,\ 9.8$ and 19.7, as shown in Fig. 5(a). The corresponding SPOD modes are presented in Fig. 7. The dominant mode at $St = 0.9$ is strongly confined within the slat cove, with negligible amplification downstream of the slat trailing edge. The leading and subdominant modes exhibit similar amplitudes and spatial patterns, suggesting a paired modal structure. This behaviour contrasts with the $Re_c = 1.270 \times 10^4$ case, where the dominant modes extend into the downstream region and reflect a more global interaction. The leading modes at $St = 9.8$ and 19.7 differ predominantly in amplitude, as shown in Fig. $7(b,c)$, while exhibiting similar spatial patterns. A comparable behavior is observed in the corresponding subdominant modes (Fig. $7(e,f)$). At $St = 9.8$, the SPOD modes exhibit alternating structures aligned with the separated shear layer originating from the slat cusp and extending toward the main-element leading edge, characteristic of a Kelvin–Helmholtz-type instability.

SUMMARY

A database of three-dimensional direct numerical simulations of incompressible flow past a 30P30N high-lift airfoil at low Reynolds numbers, Re_c, is analysed via spectral proper orthogonal decomposition (SPOD) to identify dominant coherent structures in the slat-cove region. The SPOD results exhibit clear low-rank behaviour, with well-converged leading modes ($\beta_{i,k} \sim 0.95$) capturing the dominant physical mechanisms.

At $Re_c = 1.27 \times 10^4$, the flow shows distinct narrowband peaks at low Strouhal numbers, St. The dominant mode at $St = 0.8$ extends from the slat cove downstream into region above the main element, with maximum amplitude near the interaction between the slat wake and the boundary layer close to the leading edge. Higher frequencies ($St = 1.5,\ 2.3$) exhibit similar spatial structures but with increased localization within the cove and near the slat trailing edge. At $Re_c = 1.83 \times 10^4$, the dominant low-frequency mode at $St = 0.9$ is largely confined within the slat cove, with minimal downstream amplification, indicating a shift toward a slat-cove-localized oscillatory pattern. In contrast, higher-frequency modes ($St = 9.8,\ 19.7$) exhibit convecting structures aligned with the separated shear layer from the slat cusp, consistent with Kelvin–Helmholtz instability.

Overall, the results indicate a Re_c dependence in both the dominant low- and higher-frequency structures. However, a direct link between the energetic modes and centrifugal instability associated with the Görtler vortices is not evident from the present modal analysis.

REFERENCES

Abreu, L. I., Tanarro, A., Cavalieri, André V. G., Schlatter, P., Vinuesa, R., Hanifi, A. & Henningson, D. S. 2021 Spanwise-coherent hydrodynamic waves around flat plates and airfoils. *Journal of Fluid Mechanics* **927**, A1.

Aguirre, F. O., Schmidt, O. T. & Medeiros, M. A. 2025 Spectral proper orthogonal decomposition of transitional flow over an open cavity. In *AIAA Aviation Forum and Ascend 2025*, p. 3454.

Fischer, P., Kerkemeier, S., Min, M., Lan, Y.-H., Phillips, M., Rathnayake, T., Merzari, E., Tomboulides, A., Karakus, A., Chalmers, N. *et al.* 2022 NekRS, a GPU-accelerated spectral element Navier–Stokes solver. *Parallel Computing* **114**, 102982.

Kokash, H., Mavriplis, C. & Agbaglah, G. G. 2024 On the origin of Görtler vortices in flow over a multi-element airfoil. *Journal of Experimental and Theoretical Analyses* **2** (4), 121–133.

Lin, C. & Schmidt, O. 2024 Modal decomposition of K-type boundary layer transition. In *AIAA SciTech 2024 Forum*, p. 0495.

Patera, A. T. 1984 A spectral element method for fluid dynamics: Laminar flow in a channel expansion. *Journal of Computational Physics* **54** (3), 468–488.

Sasaki, K., Morra, P., Cavalieri, A. V. G., Hanifi, A. & Henningson, D. S. 2020 On the role of actuation for the control of streaky structures in boundary layers. *Journal of Fluid Mechanics* **883**, A34.

Schmidt, O. T. & Colonius, T. 2020 Guide to spectral proper orthogonal decomposition. *AIAA Journal* **58** (3), 1023–1033.

Schmidt, O. T., Towne, A., Rigas, G., Colonius, T. & Bres, G. A. 2018 Spectral analysis of jet turbulence. *Journal of Fluid Mechanics* **855**, 953–982.

Teng, M. & Mavriplis, C. 2025 Transition to turbulence of an incompressible flow past a multi-element airfoil: Mean-flow dynamics. *International Journal of Heat and Fluid Flow* **115**, 109825.

Wang, J. S., Feng, L. H., Wang, J. J. & Li, T. 2018 Görtler vortices in low-Reynolds-number flow over multi-element airfoil. *Journal of Fluid Mechanics* **835**, 898–935.

Wang, J. S. & Wang, J. J. 2021 Wake-induced transition in the low-Reynolds-number flow over a multi-element airfoil. *Journal of Fluid Mechanics* **915**, A28.

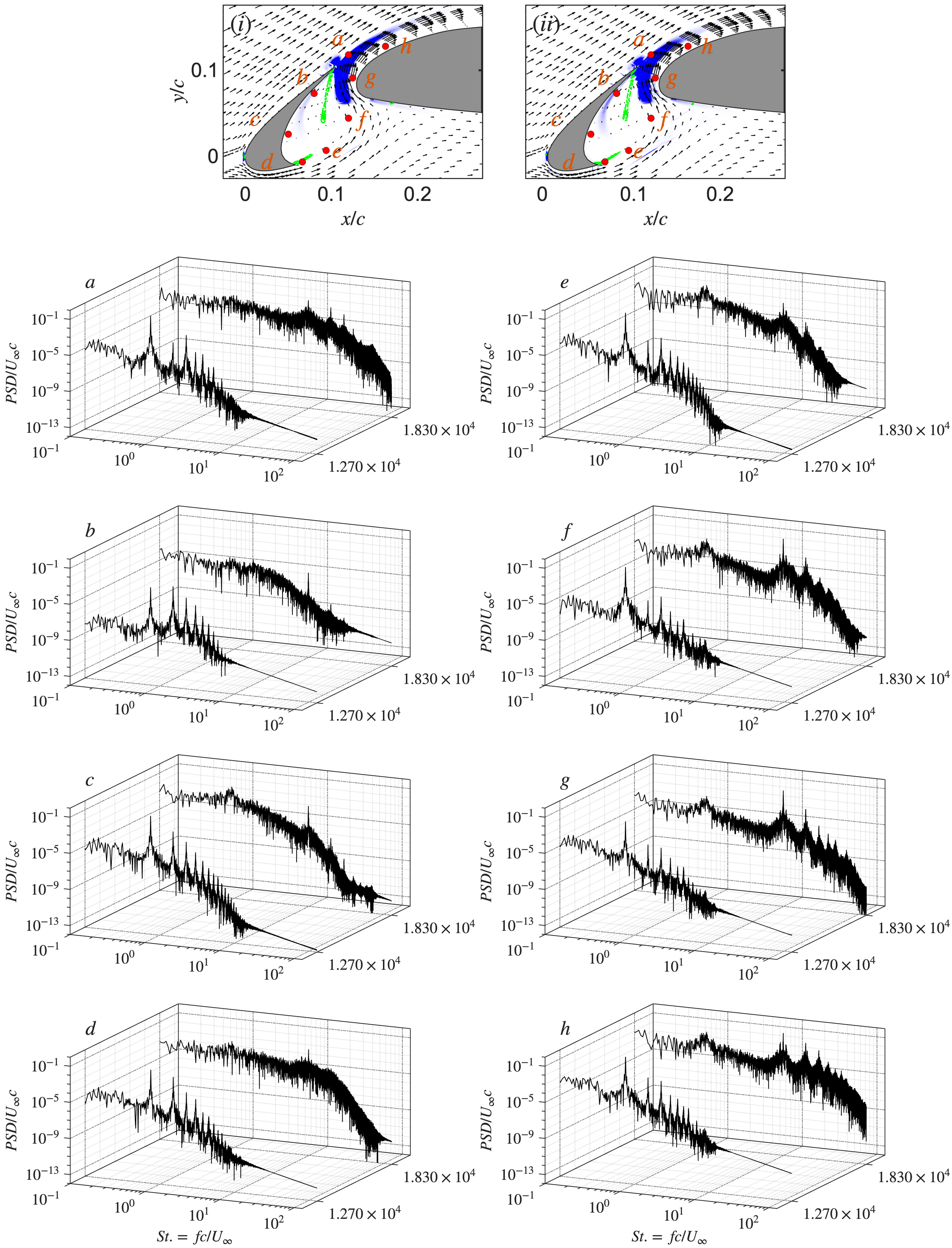

Figure 2. Normalized power spectral density (PSD) of streamwise velocity component, u, at selected spots (a through h) in the mid-plane ($z/c = 0.1$) as shown in the top figures. The inviscid Rayleigh discriminant is shown in blue and iso-contours of the Görtler number are plotted as 10 linearly spaced green dashed lines between $\frac{1}{4}G\ddot{o}_{\delta^*}|_{max}$ and $\frac{3}{4}G\ddot{o}_{\delta^*}|_{max}$ (Teng & Mavriplis, 2025). (i) $Re_c = 1.270 \times 10^4$ and (ii) $Re_c = 1.830 \times 10^4$. Black arrows indicate the mean-flow field.

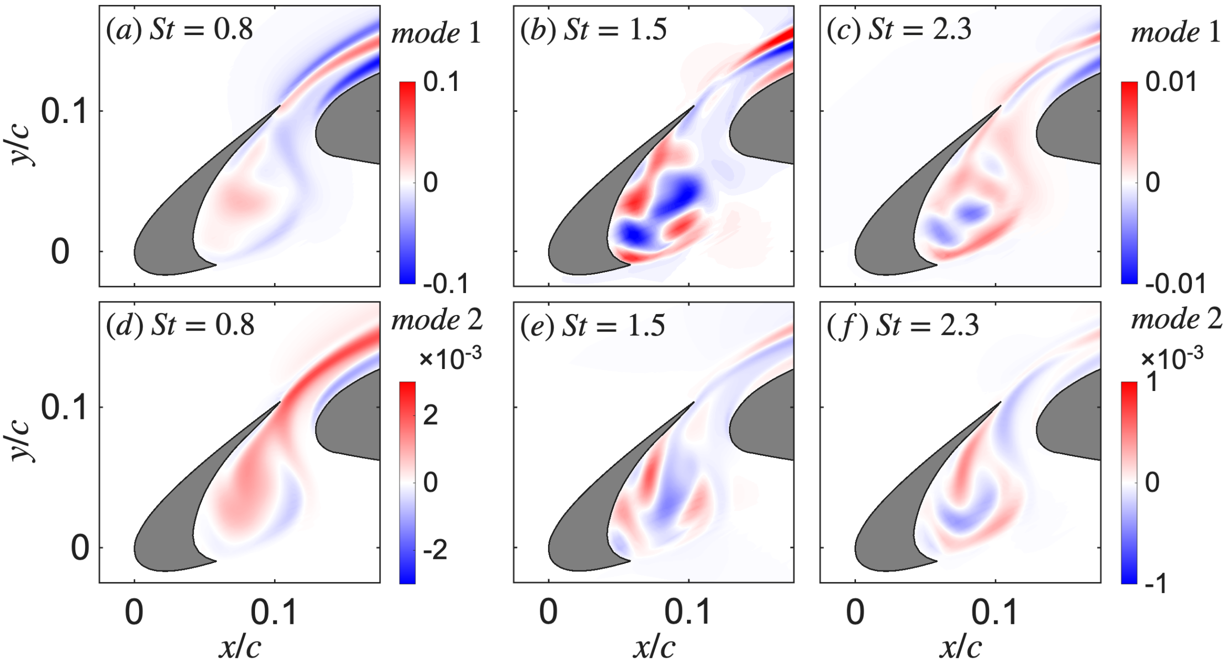

Figure 6. SPOD eigenmodes for incompressible flow in the slat-cove region of a 30P30N highlift airfoil at $Re_c = 1.270 \times 10^4$ (region shown in Fig. 1). Modes 1 and 2 are shown in the top and bottom rows for the three dominant frequencies of $St = fc/U_\infty =$ 0.8 (left), 1.5 (middle) and 2.3 (right).

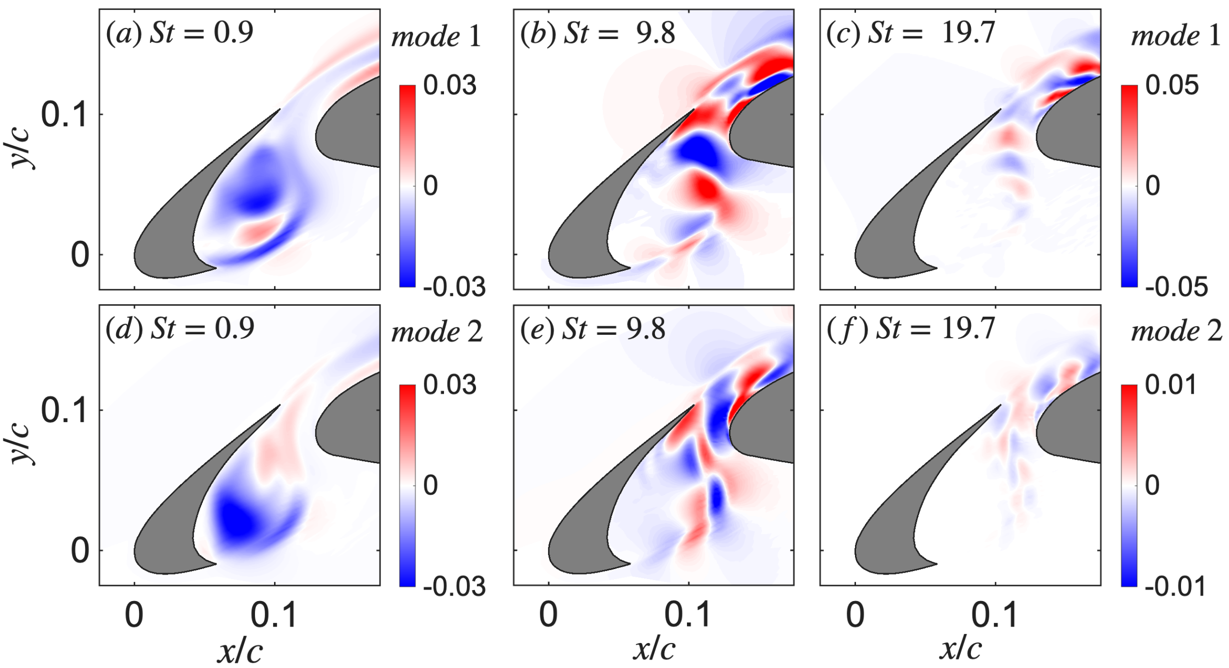

Figure 7. SPOD eigenmodes for incompressible flow in the slat-cove region of a 30P30N highlift airfoil at $Re_c = 1.830 \times 10^4$ (region shown in Fig. 1). Modes 1 and 2 are shown in the top and bottom rows for the three dominant frequencies of $St = fc/U_\infty =$ 0.9 (left), 9.8 (middle) and 19.7 (right).